INSTITUTE OF PHYSICS PUBLISHING NANOTECHNOLOGY
Nanotechnology **17** (2006) 3584–3590 doi:10.1088/0957-4484/17/14/038

Mechanical comparison of a polymer nanocomposite to a ceramic thin-film anti-reflective filter

Thad Druffel[1,3], **Kebin Geng**[2] **and Eric Grulke**[2,3]

[1] Optical Dynamics Corporation, 10100 Bluegrass Pkwy, Louisville, KY 40299, USA
[2] Department of Chemical and Materials Engineering, University of Kentucky, Lexington, KY 40506, USA

E-mail: tdruffel@opticaldynamics.com and egrulke@engr.uky.edu

Received 26 April 2006, in final form 2 June 2006
Published 26 June 2006
Online at stacks.iop.org/Nano/17/3584

Abstract
Thin-film filters on optical components have been in use for decades and, for those industries utilizing a polymer substrate, the mismatch in mechanical behaviour has caused problems. Surface damage including scratches and cracks induces haze on the optical filter, reducing the transmission of the optical article. An in-mold anti-reflective (AR) filter incorporating 1/4-wavelength thin films based on a polymer nanocomposite is outlined here and compared with a traditional vacuum deposition AR coating. Nanoindentation and nanoscratch techniques are used to evaluate the mechanical properties of the thin films. Scanning electron microscopy (SEM) images of the resulting indentations and scratches are then compared to the force deflection curves to further explain the phenomena. The traditional coatings fractured by brittle mechanisms during testing, increasing the area of failure, whereas the polymer nanocomposite gave ductile failure with less surface damage.

(Some figures in this article are in colour only in the electronic version)

1. Introduction

Thin-film optical filters have been around for over a century and chemical vapour deposition techniques have been predominately the manufacturing choice. The technique generally includes the deposition of metal oxide 1/4-wavelength thin-film layers of varying refractive index to get a change in the optical efficiency of the surface of a substrate. These can include broadband anti-reflective and reflective coatings as well as edge and band-gap filters [1]. Anti-reflection coatings over the visible spectrum (380–780 nm) are the predominant use for these filters, with uses in ophthalmic lenses, solar cells, data storage and other optical devices requiring high optical transmission.

Traditional vacuum-deposited anti-reflective coatings have been around since the 1930s and actually performed well when coated on a glass ophthalmic lens, since the coatings themselves were ceramic. During the 1970s, manufacturing improvements allowed for polymer lenses to gain general acceptance as an alternative for glass; however, anti-reflective coatings did not fair well on plastic substrates due to the major differences in the strain behaviour of the coating and the lens. Significant progress has been made in this technology, but the disparity in the strain domains continues to be an issue. Spin-on glass coatings via the sol–gel process and hybrid materials including Ormosils have also been proposed, but these have not gained acceptance in the marketplace.

Surface damage to an optical article can induce transmission losses by scattering the incident light. The light scatter is evident as haze, which increases with surface roughness and as debonding occurs. A brittle material will exhibit fracture features including voids, cracks, crazing and debonding, whereas in a ductile material, damage is smooth in nature [2]. Debonding can lead to further damage, as humidity changes further stress the interfacial boundaries. Cracks and voids can act as stress risers, giving way to further damage.

[3] Authors to whom any correspondence should be addressed.

These surface defects can also arise from large differences in the thermal expansion coefficients and ultimate strains between the layers and the substrate. Large strain domain differences can also reduce the resilience of the final article, reducing the impact resistance.

The goal of this work was to compare the mechanical performance of an anti-reflective article featuring a proprietary polymer nanocomposite system to an anti-reflective coating deposited on a polymer substrate using traditional vacuum deposition techniques. The method outlined here represents a low-cost solution to creating an anti-reflective article that more closely matches the strain performance of the anti-reflective layers to the polymer substrate. The coatings are applied to a mold in reverse order using a spin-coating technique, and then the molds are assembled to create a lens cavity. A low-viscosity monomer is introduced in between the two surfaces and cured, at which point the coatings are cured to the substrate. The molds are then removed, leaving a plastic anti-reflective article [3].

The nanocomposite layers used for this thin-film filter consist of a hybrid polymer with metal oxide nanoparticles [4–6]. The nanoparticles are used to engineer the refractive index and the mechanical properties of the layer. The in-mold method creates a chemical bond between the layers and the substrate. There has been work in which an AR coating based on sol–gel technology has been applied to an optical article using spin coating [7, 8], but these often require a higher temperature bake-out, and there remains an issue with the adhesion to the substrate.

In the last decade, nanoindentation and nanoscratch techniques have proven to be powerful tools in characterizing thin films [9, 10]. Much work has appeared on the analysis of polymer films on metal substrates [11, 12], polymer films on polymer substrates [13, 14] and multi-layered films on metal substrates [15, 16]. In this work, we consider a multi-layered film system, both organic and inorganic, on a polymer substrate, having a total thickness of approximately 300 nm. The films are compared using nanoindentation and nanoscratch tests to assess the mechanical performance of the end product. SEM images of the indentations and scratches are also presented to help explain the failures further.

2. Experimental details

2.1. Sample preparation

In order to make sure that we compared the anti-reflective thin films, both substrates were acrylic flats made by Optical Dynamics Corporation. One set was then coated using a traditional vacuum deposition technique (ceramic), having a total thickness of approximately 330 nm. A second set was made using in-mold casting technology (nanocomposite), which yields an anti-reflective thin film approximately 300 nm thick, as described in the following paragraphs.

The anti-reflective layers in the nanocomposite approach are applied to the molds in reverse order using a spin coater from Optical Dynamics Corporation. The environment of the coater is HEPA filtered to keep defects to a minimum. The machine first cleans the molds using a high-pressure water wash to remove any fine contaminates on the molds. Each layer of the stack is coated onto a glass mold using the spin-coating technique, which is a simple and efficient method for depositing uniform thin films on a substrate. The well-understood technique controls the layer thickness by balancing the centrifugal forces of a developing thin film to the viscous forces that increase as evaporation takes place [17, 18]. The repeatability of this method is extremely high, as long as the coating environment is controlled such that the evaporation rate stays constant. This is accomplished by regulating the temperature of the coating chamber and also by exhausting solvent rich air out of the coating bowl.

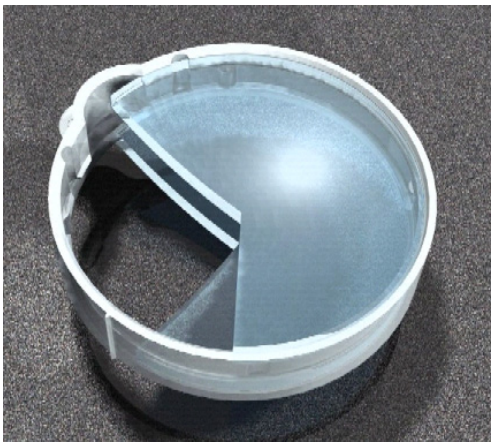

Figure 1. Mold assembly cut away to show the cavity into which the low-viscosity monomer is added. After curing, the gasket and molds are removed, leaving the final article.

After the solvent is evaporated, a thin film on the order of a 1/4 wavelength of an ultraviolet (UV)-curable monomer and nanoparticles remain. The layer is then partially cured using a pulse xenon UV source lamp, leaving a partially cured polymer nanoparticle composite. Subsequent layers are then added on top of the previous layer to build the anti-reflective stack in reverse order. Each mold is processed through the machine in about 10 min.

The reverse-coated molds are then assembled as shown in figure 1 and a low-viscosity monomer is introduced into the system. The monomer is then cured using a UV source and heat, which is a process that takes a total of 10 min. This curing process creates a very good bond between the layers and the polymer lens. When the cure is complete, the molds are removed in a water bath and the lens is cleaned and placed into a low-temperature oven and annealed. The final product has the surface qualities of the mold itself, such that the article does not need any post-processing to complete the prescription.

2.2. Sample analysis

There has been some research that indicates that surface roughness can limit the effectiveness of the assumption for the contact area of an indenter [19, 20]. In order to confirm that the surface roughness of the specimens does not violate the assumptions, the surfaces were mapped using an atomic force microscope (AFM) from Quesant (of Agoura Hills, CA, USA).

The nanoindentation tests were preformed in a Hysitron Triboscope (Minneapolis, MN, USA) using a diamond

NorthStar cubic indenter (Minneapolis, MN, USA) with a nominal tip radius of 40 nm. The indentation tests were carried out using a load control mode with indentation loads up to 6000 μN at a rate of up to 1200 μN s^{-1}. Using the methods developed by Oliver and Pharr [10], the reduced modulus E_r was calculated from

$$E_r = \frac{\sqrt{\pi}}{2\sqrt{A}} \frac{dF}{d\delta}$$

where A is the projected contact area, F is the peak load during indentation, δ is the indentation depth, and the contact stiffness is the slope $dF/d\delta$ taken at the upper portion of the unloading curve. The reduced elastic modulus is composed of elastic deformations in the specimen and the indenter and is related to the elastic modulus of the specimen by:

$$\frac{1}{E_r} = \frac{1-\nu_s^2}{E_s} + \frac{1-\nu_i^2}{E_i}$$

where the subscripts s and i refer to the specimen and the indenter, respectively, and ν and E are Poisson's ratio and the elastic modulus, respectively. Models proposed by Saha and Nix [21] further separate the film from the substrate as long as these are both stiff. To date, an adequate model separating a stiff film from a compliant substrate does not exist. However, we will not consider the film to be separate, since the substrate is the same in both cases and constitutes the final optical article. The hardness H can also be computed using the indentation from:

$$H = \frac{F_{max}}{A}$$

where F_{max} is the maximum load.

For large indentation loads, glassy materials may exhibit cracking during the indentation process [12, 22], especially for a cubic indenter where indentations exceeding 10% are expected to include the substrate [23]. There are several types of cracks that may occur during indentation. Radial cracks are common for sharp indenters and extend outward from the edges of the indenter, and cone cracks occur circumferentially around the indentation. These fractures are evident as sharp changes in the slope of the force displacement curves during the indentation. This stiffness will have large discontinuities as strain energy is released during fractures. The AFM attached to the indenter does not have the resolution to depict accurately any cracking that may have occurred, so the indentation was analysed using a Hitachi-3200 SEM. There are several models for the computation of the fracture toughness based on the size of the crack dimensions [12] or as the projected area of the force–displacement curve [23]. We will only consider the critical load at which cracking occurs, which is seen as a discontinuity in the load–displacement curve during indentation.

Nanoscratch tests were preformed in a Hysitron Triboscope using a diamond NorthStar cubic indenter with a nominal tip radius of 40 nm. The scratch was made with one sharp edge of the indenter oriented in the direction of travel (point-on orientation) and the applied normal load was increased linearly to the maximum load (ramp mode) with the indenter moving along at a speed of 1/3 μm s^{-1}. The maximum scratching distance was 10 μm. The normal and lateral forces of the indenter were monitored during scratching, with specific attention

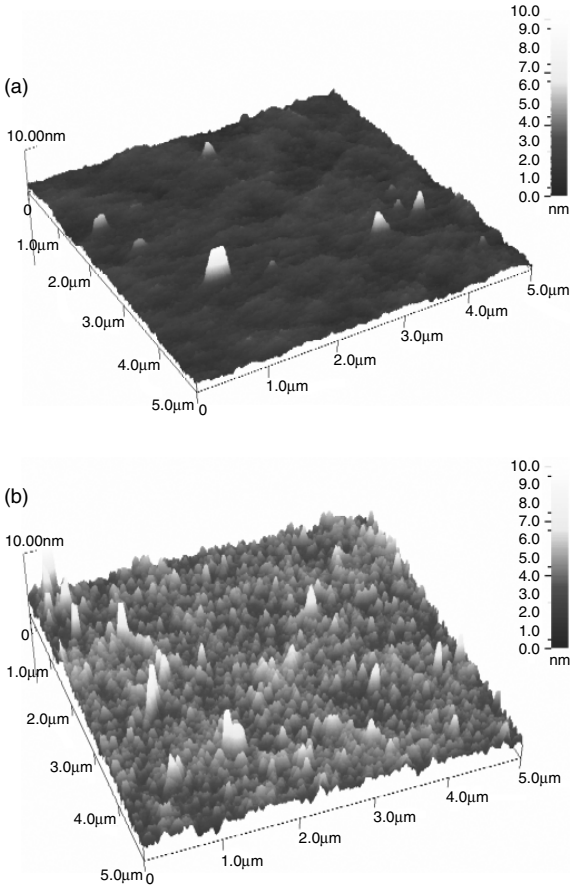

Figure 2. AFM Surface maps of (a) the nanocomposite sample (R_a: 4.00 nm) and (b) the ceramic sample (R_a: 6.42 nm). The surface roughness (R_a) is the average deviation of surface height from the mean plane.

to discontinuities in the lateral force curve, indicating stresses exceeding the yield and ultimate stresses.

The stress distribution during a scratch has been detailed by Xiang and indicates a sharp increase in the tensile stresses on the trailing end of the stylus [2]. Again, a glassy material does not exhibit high tensile strength, and we would expect to see tensile failures along with shear rupture during a scratch. The two types of failure expected during the scratch for glassy materials are ductile and brittle [24, 25]. In plastic failure, the material is strained beyond the yielding limit in shear and should leave a relatively smooth scratch, although there may be some tearing. A brittle failure pushes the stresses beyond the tensile yield and will exhibit sharp cracks in the trough as well as a very rough lateral force scan. The fracture mechanisms are well detailed by Li and Bhushan [26, 27] and here we provide SEM images for visual comparison.

3. Results and discussion

Images from the AFM depicting the surface roughness of the two films are shown in figure 2. The columnar surface profile of the traditional vacuum deposition is evident in the image, but the surface roughness of each sample is on the order of a few nanometres and should not affect the indentation

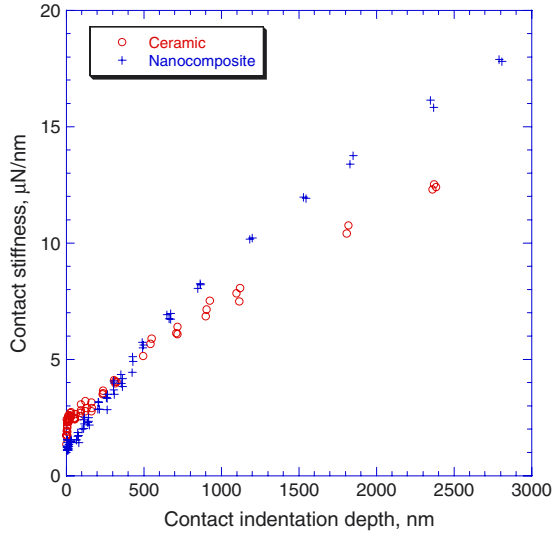

Figure 3. The contact stiffness of the two samples as a function of indentation depth.

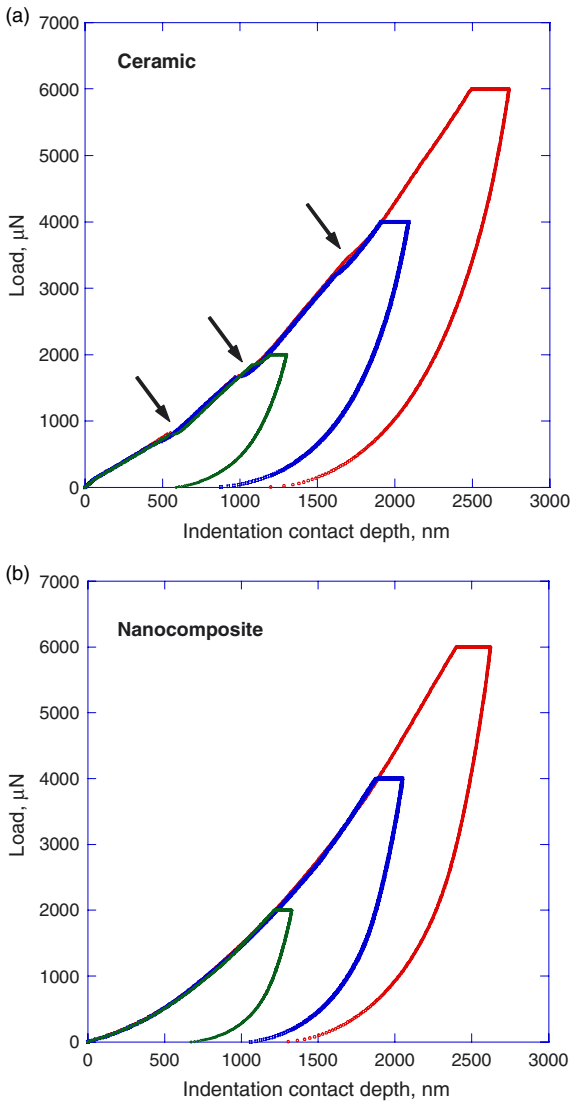

Figure 4. Load–displacement curves from nanoindentation for (a) the ceramic sample and (b) the nanocomposite sample.

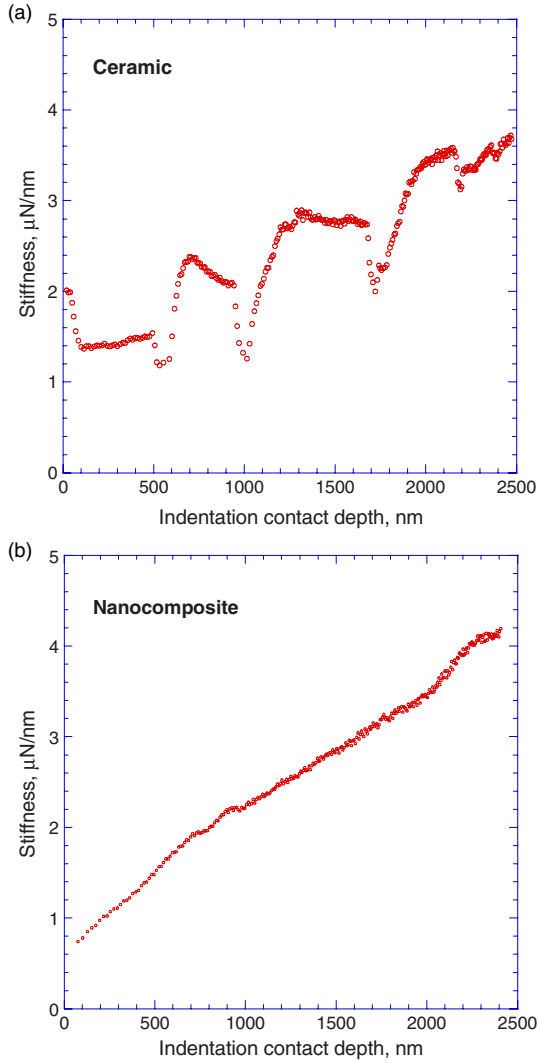

Figure 5. Stiffness of (a) the ceramic and (b) the nanocomposite sample at an indentation load of 6000 μN.

and scratch tests [25]. The average surface roughness R_a (the deviation of surface height from the mean plane) of the polymer nanocomposite film was 4.00 nm (figure 2(a)) and 6.42 nm for the vacuum-deposited ceramic film (figure 2(b)).

Several nanoindentations were performed on each sample and the response of the contact stiffness against the indentation contact depth was plotted (figure 3). As expected at low indentation depths, the contact stiffness of the ceramic is higher; however, as the indentations exceed the film thickness, the graph bends and the contact stiffness of the nanocomposite is greater. The modulus of elasticity and the hardness of the films were calculated at indentation depths of 29.4 nm for the ceramic and 32.5 nm for the nanocomposite. Poisson's ratio of the ceramic and nanocomposite were assumed to be 0.2 and 0.4, respectively. The modulus of elasticity of the ceramic coating is 13.2 GPa and for the nanocomposite it is 6.32 GPa, and the hardness for the ceramic coating is 3.6 GPa and for the nanocomposite it is 0.83 GPa. The ceramic sample is over four times as hard, which is not a surprising result; what is interesting to note is that the comparison of the bulk properties of the materials does not line up with those measured here.

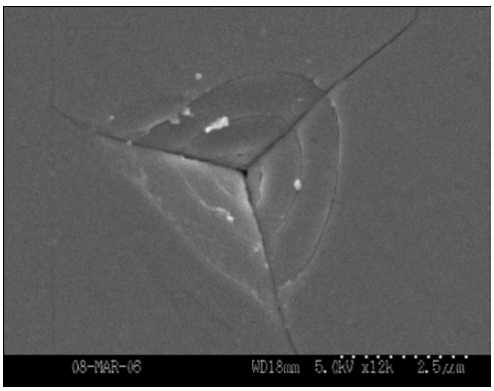

(a)

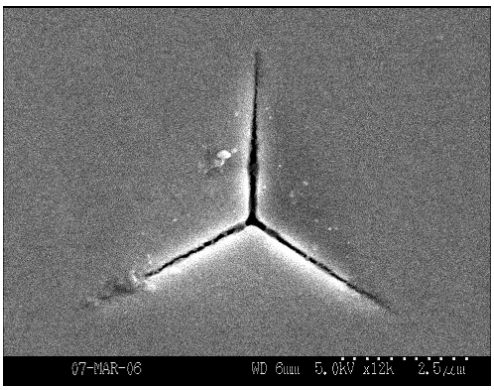

(b)

Figure 6. SEM images of indentation for (a) the ceramic sample and (b) the nanocomposite sample at an indentation load of 6000 μN.

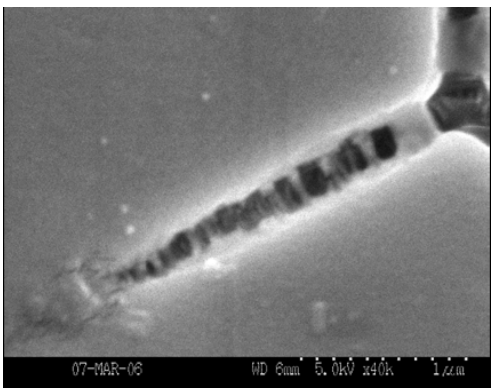

Figure 7. Close-up of the nanocomposite indentation.

This can be explained by the relatively soft substrate, which we included in the analysis, as it is a part of the finished article and, as such, needs to be included. The results of the contact stiffness suggests that, at large indentations, the ceramic film no longer supports the indenter due to fracture, thus the increased hardness of the film does not yield an advantage and, as discussed further, may be a drawback.

The more interesting data from the nanoindentation are the load–displacement curves (figure 4), in which the ceramic sample shows several discontinuities during the loading phase that can be attributed to a brittle failure (figure 4(a)). This indentation-induced failure consistently occurs at the multiple

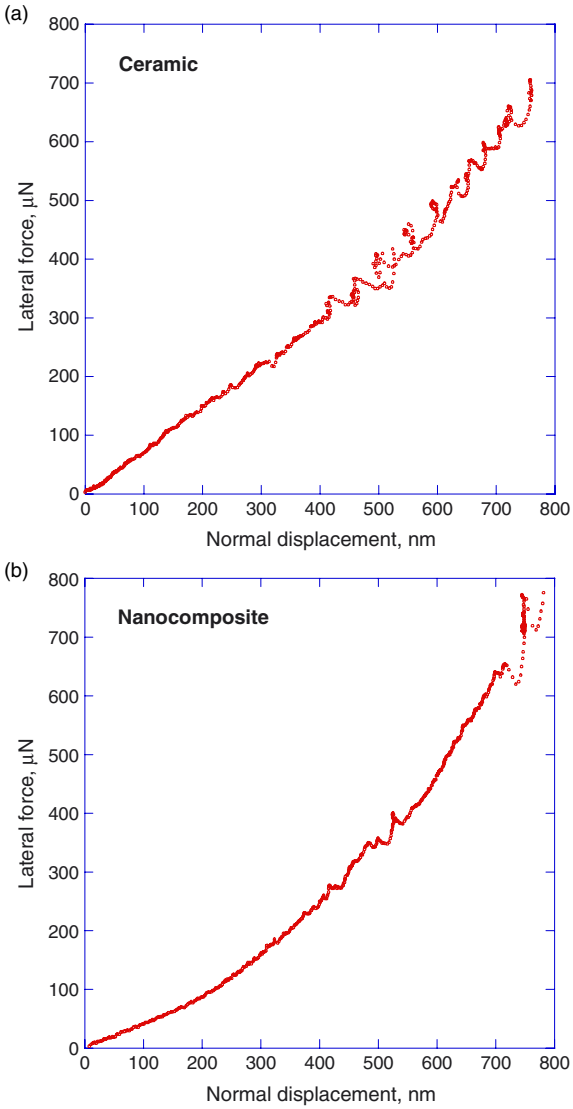

Figure 8. Nanoscratch lateral force curve for (a) the ceramic sample and (b) the nanocomposite sample at the maximum load of 1000 μN as a function of the scratch depth.

penetration depths of around 530, 1020, 1720 and 2200 nm. These are more clearly illustrated by the stiffness curve as a function of indentation depth (figure 5(a)). This failure does not show up with the nanocomposite sample (figure 4(b)) and, to make sure that it was not hidden, we also took the derivative of the loading curve to determine if there is a jump in the stiffness, which we do not see (figure 5(b)). From this, we can infer that the failure does not occur in the substrate, but rather is a fracture of the film.

In order to verify the cracking behaviour, the samples were analysed under an SEM, as shown in figure 6. The nanocomposite sample shows no cracking, either radially from the edges of the cubic indenter or concentrically around the point of indentation (figure 6(b)). From these results and the load displacement curves, we can say with much certainty that the indentation is purely plastic/elastic and that there is no delamination from the substrate. The ceramic sample does show cracks emanating radially outward from the edges of the

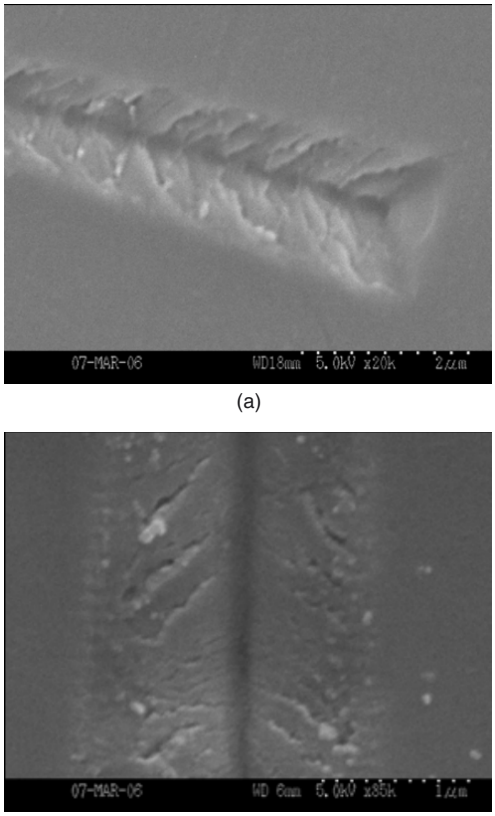

Figure 9. SEM images of scratch for (a) the ceramic sample and (b) the nanocomposite sample.

indenter as well as circumferential cracks (figure 6(a)). We cannot determine from this data whether the zone cracking has initiated a delamination, although, due to the probable strain density at the interface, this is probable.

The other interesting phenomenon exhibited by the nanocomposite sample is the elastic response to the indentation. Upon closer focus of the indentation (figure 7), we noticed that, at the edge of the tip, there is some localized plastic failure with elastic recovery. This is quite interesting, in that the nanocomposite sample exhibits the ability to absorb the indentation elastically without a failure.

Nanoscratch tests showed a very similar response: the response of the nanocomposite sample was purely plastic/elastic and the ceramic sample exhibited brittle failures. In each case, the lateral force curves show deviation from the linearly applied normal force (figure 8). The reduction in the lateral force is attributed directly to the release of strain energy due to a plastic or brittle failure. The ceramic sample exhibits much sharper transitions in the lateral forces that increase in period as the scratch load is increased and consequently the normal displacement (the penetration depth) increases (figure 8(a)). This would be expected of a ceramic material with small ultimate strains, causing tensile failures at the trailing edge of the stylus. The elastic response of the nanocomposite sample has a smoother lateral force curve (figure 8(b)).

As with the indentations, we took images of the scratch using an SEM to confirm the response (figure 9). The ceramic sample exhibits a classic snapshot of brittle cracking due to tensile failures at the trailing edge of the indenter (figure 9(a)). The nanocomposite exhibits failures that look plastic in nature; in other words, the bottom of the trough is straight with a rough edge (figure 9(b)).

4. Conclusions

In this study, we have compared the mechanical response of a newer technology for applying an anti-reflective thin-film filter on an optical article to a well-established technology. In particular, we have concentrated on common surface failures to the final product which include scratching, delamination and crazing (which commonly occurs with rapid strain fluctuations). These failures lead to light scatter, which reduces the optical efficiencies of the thin-film filters. In this study, the ceramic film fractured via a brittle mechanisms, increasing the scope of the failure, whereas the nanocomposite gave a ductile failure with less surface damage. The newer technology outlined here is designed to match the elastic properties of the substrate more closely, thus eliminating many of these issues, minimizing damage done to the final article.

References

[1] Macleod H A 2001 *Thin Film Optical Filters* (London: Institute of Physics) p 641
[2] Xiang C, Sue H-J and Coleman B 2001 Scratch behavior and material property relationship in polymers *J. Polym. Sci.* B **39** 47–59
[3] Buazza O M and Sun X 2003 *Method of Forming Antireflective Coatings* (United States: Q2100, Inc)
[4] Mennig M, Oliveira P W and Schmidt H 1999 Interference coatings on glass based on photopolymerizable nanomer material *Thin Solid Films* **351** 99–102
[5] Mennig M *et al* 1999 Multilayer NIR reflective coatings on transparent plastic substrates from photopolymerizable nanoparticulate sols *Thin Solid Films* **351** 225–9
[6] Krogman K, Druffel T and Sunkara M 2005 Anti-reflective optical coatings incorporating nanoparticles *Nanotechnology* **16** S338–43
[7] Oliveira P W *et al* 1997 Generation of wet-chemical AR coatings on plastic substrates by the use of polymerizable nanoparticles *Sol–Gel Optics IV* (San Diego, CA: SPIE)
[8] Imai H *et al* 1997 Densification of sol–gel thin films by ultraviolet and vacuum ultraviolet irradiations. *J. Sol-Gel Sci. Technol.* **8** 365–9
[9] Bushan B and Li X 2003 Nanomechanical characterisation of solid surfaces and thin films *Int. Mater. Rev.* **48** 125–64
[10] Oliver W C and Pharr G M 1992 An improved technique for determining hardness and elastic modulus using load and displacement sensing indentation experiments *J. Mater. Res.* **7** 1564–83
[11] Geng K *et al* 2005 Nanoindentation behavior of ultrathin polymeric films *Polymer* **46** 11768–72
[12] Malzbender J *et al* 2002 Measuring mechanical properties of coatings: a methodology applied to nanoparticle-filled sol–gel coatings on glass *Mater. Sci. Eng.* R **36** 47–103
[13] Charitidis C *et al* 2004 Comparison of the nanomechanical and nanoscratch performance of antiscratch layers on organic lenses *Surf. Coat. Technol.* **180/181** 357–61
[14] Soloukhin V A *et al* 2002 Mechanical properties of silica-(meth)acrylate hybrid coatings on polycarbonate substrate *Polymer* **43** 6169–81
[15] Chudoba T *et al* 2000 Determination of mechanical film properties of a bilayer system due to elastic indentation measurements with a spherical indenter *Thin Solid Films* **377/378** 366–72

[16] Gao H, Chiu C-H and Lee J 1992 Elastic contact versus indentation modeling of multi-layered materials *Int. J. Solids Struct.* **29** 2471–92
[17] Bornside D E, Macosko C W and Scriven L E 1989 Spin coating: one-dimensional model *J. Appl. Phys.* **66** 5185–93
[18] Meyerhofer D 1978 Characteristics of resists films produced by spinning *J. Appl. Phys.* **49** 3993–7
[19] Bouzakis K-D *et al* 2002 The effect of specimen roughness and indenter tip geometry on the determination accuracy of thin hard coatings stress–strain laws by nanoindentation *Mater. Charact.* **49** 149–56
[20] Han S M, Saha R and Nix W D 2006 Determining hardness of thin films in elastically mismatched film-on-substrate systems using nanoindentation *Acta Mater.* **54** 1571–81
[21] Saha R and Nix W D 2002 Effects of the substrate on the determination of thin film mechanical properties by nanoindentation *Acta Mater.* **50** 23–38
[22] Rhee Y-W *et al* 2002 Contact-induced damage in ceramic coatings on compliant substrates: fracture mechanics and design *J. Am. Ceram. Soc.* **83** 1066–72
[23] Li X and Bushan B 1997 Fracture mechanisms of thin amorphous carbon films in nanoindentation *Acta Mater.* **45** 4453–61
[24] Briscoe B J *et al* 1996 Scratching maps for polymers *Wear* **200** 137–47
[25] Wong J S S *et al* 2004 Scratch damage of polymers in nanoscale *Acta Mater.* **52** 431–43
[26] Li X and Bhushan B 2002 A review of nanoindentation continuous stiffness measurement technique and its applications *Mater. Charact.* **48** 11–36
[27] Li X and Bushan B 1999 Micro/nanomechanical and tribological characterization of ultrathin amorphous carbon coatings *J. Mater. Res.* **14** 2328–37